J Nanopart Res (2014) 16:2351
DOI 10.1007/s11051-014-2351-0

RESEARCH PAPER

Computer study of the Raman spectra and infrared optical properties of gallium nitride and gallium arsenic nanoparticles with SiO_2 core and shell

Alexander Y. Galashev

Received: 22 February 2013 / Accepted: 5 March 2014

Abstract The $J(\omega)$ Raman spectra of the $(GaN)_{129}$, $(SiO_2)_{86}$, and $(GaN)_{54}(SiO_2)_{50}$ nanoparticles as well as the optical properties of silicon dioxide and gallium arsenide nanoparticles and the four-component particles based on them were calculated using the molecular dynamics method. The spectrum of $(SiO_2)_{86}$ had three broad bands only, whereas the Raman spectrum of $(GaN)_{129}$ contained a large number of overlapping bands. The shape of Raman spectra for four-component particles depends strongly on the way the GaN-, GaAs-, and SiO_2-components are located in the nanoparticle. Increasing the temperature (from 300 K upto 1500 K) of nanoparticles causes a significant rise in the intensity of the Raman spectrum. Thus, the odd $J(\omega)$-spectrum peaks for the nanoparticle with the SiO_2-core shift in opposite directions, but this heating does not lead to the shift of $J(\omega)$-spectrum peaks for the $(GaAs)_{54}(SiO_2)_{50}$ nanoparticle with SiO_2-coating. The refractive index and absorption coefficient as well as the number of optically active electrons depend weakly on the arrangement of the conductor (GaAs) and isolator (SiO_2) in the nanoparticle.

A. Y. Galashev (✉)
Ural Division, Institute of Industrial Ecology, Russian Academy of Sciences, Sofia Kovalevskaya Str., 20, Yekaterinburg 620990, Russia
e-mail: galashev@ecko.uran.ru

Keywords Gallium arsenide · Gallium nitride · IR and Raman spectra · Nanoparticle · Silicon dioxide · Modeling and simulation

Introduction

Silicon dioxide is an essential material for technical application (Metin et al. 2011). It is used in optical and fiber devices and in microelectronics (e.g., metal-oxide semiconductor transistors). Silicon dioxide has many crystal forms: quartz, cristobalite, tridymite, and stishovite. But the best-known form is amorphous silicon dioxide. This form can be produced in the purest state. These forms of SiO_2 have SiO_4 as a base unit, where every Si atom is coordinated with four O atoms forming a tetrahedron, and every atom of oxygen serves as a bridge bonding two tetrahedrons. In various forms of SiO_2, the tetrahedrons are bonded in a variety of ways. This binding in α-quartz and amorphous silicon dioxide is almost identical. In α-quartz, the length of the bond Si–O is estimated at 1.61 Å and the angle Si–O–Si is estimated at 144°. In amorphous SiO_2, the Si–O–Si– bonds range from 1.55 to 1.65 Å as the angle varies from 136° to 180°. Experimental data of the SiO_2 nanoparticles with different sizes (diameters from 40 to 7 nm) show that the variability of the spectral features of the matrix related Raman and IR bands in the nanoparticles is above the one observed for the bulk systems before any treatments (Agnello et al. 2013). The peaks at 440, 605, 800, and

Published online: 22 March 2014

1,060 cm^{-1} in the Raman spectra of the nanoparticles at room temperature are detected (Alessi et al. 2013). The higher is the specific surface, the larger is the differences between the Raman activities of the nanoparticle and of the bulk systems.

Raman scattering is a powerful and widely used method for studying admixtures and defects in materials. This technique is used to rapidly identify materials. Because of high sensitivity of vibrational frequencies and scattering intensities to small differences in crystal structure, this method is successfully used to reveal polymorphism of materials (Bhattacharya et al. 2011). Raman spectroscopy cannot, however, be used to determine the type of vibrations (longitudinal or transverse) to which a band is related. Micro-Raman measurements over the frequency range $50 \leq \omega \leq 1{,}250$ cm^{-1} revealed the presence of several intense bands characteristic of pure SiO_2 samples. The most intense peaks are situated at 129, 220, and 501 cm^{-1} (McMillan and Hess 1990). Less intense bands at 250–480, 650–850, and 1,040–1,210 cm^{-1} were, however, also observed. Asymmetric and less intense bands and also a peak at 220 cm^{-1} likely appear because of mode overlapping (Jayaraman et al. 1987). The presence of low energy Raman lines localized between 95 and 250 cm^{-1} in GaN grown by molecular beam epitaxy was for the first time observed in (Ramsteiner et al. 1996). According to (Siegle et al. 1997a), these peaks are only present in the spectra of GaN and GaAs. It was reported in (Jiang et al. 1998) that these peaks were also characteristic of GaN layers grown by molecular beam epitaxy on sapphire and GaAs substrates. Their intensity decreased as the temperature increased, and they completely disappeared at room temperature. They were therefore assigned to electronic excitation of donors. More recent measurements in a magnetic field at a high pressure, however, showed that all the lines were caused by vibrational Raman scattering, and their temperature dependence was caused by a resonance process (Siegle et al. 1998). Theoretical calculations showed that these lines were related to as admixtures in GaN (Kaczmarczyk et al. 2000). Semiconductors contain many electronic excitations thanks to free and bound charges. Electronic excitations can be related to lattice vibrations. The influence of free charge carriers on Raman spectra and their relation to longitudinal optical phonons was considered in (Kozawa et al. 1994) for the example of *N*-type GaN films.

It was shown experimentally that, because of epitaxial growth of GaN at 293–1,373 K brought in contact with SiO_2, compression and shear stresses appeared close to bases of growing GaN pyramids (Zheleva et al. 1999). These stresses had maximum values of 3 and 0.9 GPa, respectively. They were caused by different thermal expansion coefficients of GaN and SiO_2. An analysis of the field of stresses using the method of finite elements allowed the geometric conditions of experiment necessary for the obtainment of the required morphology characteristics of GaN crystals to be predicted and optimized.

The structure of materials is usually determined from Bragg peaks in their diffraction patterns. Fine powders, however, do not possess extended structural coherence of usual crystals and give diffraction patterns with a well-defined diffusion component and several broad Bragg-like special features. For this reason, the traditional diffraction technique is very difficult to use for structure determination. Raman scattering from nanoparticles whose size is smaller than 5 nm has not been studied as yet. Such studies can, however, be performed using computer experiments.

Nanoparticles have typical colloidal properties. The most characteristic one is the high percentage of atoms occupying the nanoparticle surface. The surface atoms have unsaturated bonds, and hence can bind to the other atoms; i.e., they have high chemical activity. The particle size, surface condition, and interatomic interaction specify the unique properties of nanoparticles and make potential application of them in many fields possible (Okuyama and Lenggoro 2003; Vassileva and Furuta 2001).

The amorphous GaAs has good optical and electronic properties. Considerable efforts go into producing the crystal GaAs. Nano-GaAs acquires new properties, opening up of fresh opportunities for technical applications and widespread use of these materials. GaAs nanocrystals (having sizes in the range of 7–15 nm) have been synthesized by an electrochemical route from the acidic solutions of metallic gallium and arsenic oxide (Nayak et al. 2004). Structural analysis by transmission electron microscopy reveals the presence of orthorhombic phase, in contrast to the usual cubic phase of bulk GaAs. Micro-Raman analysis shows a phonon mode centered at 250 cm^{-1} associated with a point defect. On the spectra from the wires, two peaks can be clearly observed. The peak positioned at 268.7 cm^{-1} is due to

scattering from the transverse-optical (TO) phonon and the peak positioned at 292.2 cm^{-1} is due to scattering from the longitudinal-optical (LO) phonon (Mooradian and Wright 1966). The Raman phonon modes of nanowires to the known bulk GaAs (1 0 0) phonon modes have been compared. In general, the phonon modes showed down shift, asymmetrical broadening, and intensity ratio of LO/TO less than 1. The down shift in Raman modes can been attributed to lattice defects (Bailon-Somintac et al. 2011).

The GaAs films are deposited on various substrates, e.g., on Si. But for practical application, in many cases, SiO_2 is more preferable as a substrate. For nanoparticles, the SiO_2 coating is more commonly deposited outside the particle. This considerably increases the thermal stability of the nanoparticle, due to the fact that the melting temperature of SiO_2 ranges from 1,873 to 1,998 K. The energy structure of the InAs/GaAs and InAs/InGaAs/GaAs systems is considered in (Bouzaïene et al. 2011; Kim et al. 2006). The process of generating point and cluster defects both in the volume system of GaAs and in the thin films of GaAs was investigated in (Nordlund et al. 2000) by the molecular dynamics method. While irradiating GaAs with high-speed ions, most of the defects were shown to be generated near the ions, but the biggest cluster defects can be generated along the route of the bombarding ions. The optical and dielectric properties of the nanoparticles of GaAs covered with SiO_2 have not been investigated to date, and the nanoparticles $(SiO_2)_n$ and $(GaAs)_m$ with inverted placement of components (GaAs is outside) were not produced. The molecular dynamic calculations (Tersoff 1986, 1989; Munetoh et al. 2007; Nishidate and Nikishkov 2008; Billeter et al. 2006) suggest that the Tersoff potential can adequately reproduce the physical properties of a multicomponent system.

The purpose of this work was to use the molecular dynamics method for obtaining the Raman spectra of the $(GaN)_{129}$, $(SiO_2)_{86}$, and $(GaN)_{54}(SiO_2)_{50}$ nanoparticles. The $(GaN)_{54}(SiO_2)_{50}$ nanoparticle was represented by species of two types: a GaN particle covered by a SiO_2 layer and a SiO_2 particle with a GaN layer deposited on it. Our main concern also is investigating the infrared and Raman spectra of the nanoparticles $(SiO_2)_n$ and $(GaAs)_m$, the SiO_2-base being both inside and outside the nanoparticle, and specifying the frequency dependence of the refraction index η and the absorption coefficient κ of such nanoparticles in the temperature range of $300 \le T \le 1{,}500$ K.

Model

The potential of the Tersoff type has limited ability to reveal the differences in chemical interaction, but it defines the chemical differences of the valency s and p electron properties. This potential is an effective instrument for modeling new materials. The Tersoff potential is based on the concept of bond order. The interatomic potential energy of two neighboring atoms i and j is written as (Tersoff 1989)

$$V_{ij} = f_C(r_{ij})\left[Aa_{ij}\exp(-\lambda^{(1)}r_{ij}) - \chi B b_{ij}\exp(-\lambda^{(2)}r_{ij})\right], \tag{1}$$

$$f_C(r_{ij}) = \begin{cases} 1, & r_{ij} < R^{(1)} \\ \frac{1}{2} + \frac{1}{2}\cos\left[\pi\dfrac{r_{ij}-R^{(1)}}{R^{(2)}-R^{(1)}}\right], & R^{(1)} < r_{ij} \le R^{(2)} \\ 0 & r_{ij} > R^{(2)} \end{cases} \tag{2}$$

where b_{ij} is the many-particle parameter of bond order (3), specifying the creation of bonding energy (the attractive part of V_{ij}) in the case of local atom distribution in the presence of other neighboring atoms (k-atoms). The potential energy is a many-particle function of positions of the atoms i, j, and k, and it is influenced by the parameters

$$b_{ij} = (1 + \xi_{ij}^{n_i})^{-1/(2n)}, \tag{3}$$

$$\xi_{ij} = \sum_{k\neq i,j} f_c(r_{ij})\beta_i g(\theta_{ijk})\exp\left[\lambda_3^3(r_{ij}-r_{ik})^3\right], \tag{4}$$

$$g(\theta) = 1 + \frac{c^2}{d^2} - \frac{c^2}{\left[d^2 + (h-\cos\theta)^2\right]}, \tag{5}$$

$$a_{ij} = (1 + \gamma^n \eta_{ij}^{n_i})^{-1/(2n)}, \tag{6}$$

$$\eta_{ij} = \sum_{k\neq i,j} f_c(r_{ij})\exp\left[\lambda_3^3(r_{ij}-r_{ik})^3\right], \tag{7}$$

$$\lambda_{ij}^{(k)} = (\lambda_i^{(k)} + \lambda_j^{(k)})/2;\ A_{ij} = (A_i A_j)^{1/2};$$
$$B_{ij} = (B_i B_j)^{1/2};\ R^{(1)} = R - D;\ R^{(2)} = R + D; \tag{8}$$

$$R_{ij}^{(1)} = (R_i^{(1)} R_j^{(1)})^{1/2};\ R_{ij}^{(2)} = (R_i^{(2)} R_j^{(2)})^{1/2}.$$

Table 1 Tersoff potential parameters

Parameter	Silicon[a]	Oxygen[a]	Gallium[b]	Nitrogen[c]	Arsenic[b]
A, eV	1803.79	1882.55	2543.2972	6368.21	1571.86084
B, eV	471.195	218.787	314.45966	511.205	546.4316579
λ_1, Å^{-1}	2.4799	4.17108	2.50842747	5.60181	2.384132239
λ_2, Å^{-1}	1.7322	2.35692	1.490824	3.16170	1.7287263
$R^{(1)}$, Å	2.5	2.7	3.4	1.75256	3.4
$R^{(2)}$, Å	2.8	3.0	3.6	2.41523	3.6
β	1.1×10^{-6}	1.1632×10^{-7}	0.23586237	4.4422×10^{-3}	0.00748809
n	0.78734	1.04968	3.4729041	2.42635	0.60879133
h	−0.59825	−0.845922	7.1459174	−0.52909	0.15292354
c	1.0039×10^5	6.46921×10^4	0.07629773	2.2955×10^4	5.273131
d	16.217	4.11127	19.796474	24.78674	0.75102662
χ	1	1	1	1	1

[a] (Munetoh et al. 2007)

[b] (Nishidate and Nikishkov 2008)

[c] (Billeter et al. 2006)

where ξ is the effective coordination number; $g(\theta)$ is the function of the angle between r_{ij} and r_{ik} that stabilizes the tetrahedral structure; and λ_3 and γ are set equal to zero.

The potential defined by Eqs. (1)–(7) is differentiated from the corresponding potential of the single-component system (Tersoff 1986) by introducing one additional parameter χ. This parameter amplifies or attenuates the heteropolar bonds with respect to the value obtained by simple interpolation. Thus, the "chemistry" is involved in this parameter or it is taken into account on choosing the interpolation formula. Here, $\chi_{ii} = 1$ and $\chi_{ij} = \chi_{ji}$, so only one independent parameter is required for a pair of two atom types. The parameter β in Eq. (4) is involved for getting additional flexibility, which is typical for the pair made up of the atoms of essentially different types.

The parameters of the Tersoff potentials for silicon, oxygen, gallium, nitrogen, and arsenic are tabulated in the Table 1 (Munetoh et al. 2007; Nishidate and Nikishkov 2008; Billeter et al. 2006). Here, the deficiently physically justified parameter χ_{ij} is assumed equal to one. The procedure of adjusting parameters with using the original Tersoff potential is presented in (Yasukawa 1996). The Tersoff potential is well transferable for the bond orbitals; the parameters fitted for sp^3-hybridization can be used for the description of interaction in the materials with sp^2-hybridization (Galashev 2010; Benkabou et al. 2003).

The initial configurations of nanoparticles were made by cutting the spheres and spherical layers out of the crystals of GaN (GaAs) with the wurtzite (zinc blende) crystal structure and the crystal of α-quartz. The previously built crystal of GaN (GaAs) was specified by the parameters: $a = b = 0.386$ nm and $c = 0.5186$ nm ($a = 0.5653$ nm) (Goldman et al. 1996). The packing of SiO_4-tetrahedrons for obtaining the crystal of α-quartz with the parameters a, $b = 0.5082$ nm, $c = 0.55278$ nm (Tersoff 1986) was generated by the program generator of mineral crystal structures GRINSP (Le Bail 2005). The four-component particle was built by surrounding a sphere consisting of one type of base units by a layer of the other atomic units. In order to obtain the nanoparticles of the first type, a sphere of SiO_2 was inserted into the spherical layer of GaN (GaAs), aligning their centers. Producing the nanoparticle of the second type included analogous attachment of the sphere of GaN (GaAs) to the spherical layer of SiO_2. In both cases, in the region of interfacing the sphere and the layer surrounding it, the base units of the spherical layer, the atoms of which were closer to any atom of the sphere than a certain selected value r_m, were removed. As a result, after assembling the nanoparticles, the minimal spacing between the atoms of different types ranged between 0.33 and 0.36 nm. The required quantity of base units of each type remained outside in the vicinity, while the atoms located farther than the

others from the center of mass of the created nanoparticle were removed. Finally, depending on its composition, the nanoparticle contained 86 base units of SiO_2, or 129 base units of GaN (GaAs), or 50 base units of SiO_2 and 54 base units of GaN (GaAs). Thus, simulations were done in a spherical model containing 258 atoms under non-periodic boundary conditions. The size of nanoparticles containing SiO_2 was within the range of 3.0–3.6 nm. The calculation of physical properties was performed by the classical molecular-dynamic ensemble representing the special case of a microcanonical ensemble. Integration of the equations of motion was performed by the Runge–Kutta method of the 4th order with the time step $\Delta t = 10^{-16}$ s. In the preliminary stage of calculation with duration of 1,00,000 Δt, the correction of the velocities of atoms was performed in order to balance the systems at a given temperature. The major calculation was made without any correction and lasted for 10^6 time steps. The molecular-dynamic (MD) calculations for every nanoparticle, I $(SiO_2)_{86}$, II $(GaN)_{129}$, III $(GaAs)_{129}$, $(SiO_2)_{50}(GaN)_{54}$ and $(SiO_2)_{50}(GaAs)_{54}$ with interior (IV, VI) and surface (V, VII) placement of SiO_2, were performed at temperature 300 K. Besides spectral properties of nanoparticles I, III, VI, and VII were investigated at temperatures of 900 and 1,500 K. The configurations of the nanoparticles, produced at low temperatures, were used in the calculations at higher temperatures.

Dielectric properties

The calculation of the dielectric properties of two- and four-component particles based on them differs from the calculation of the corresponding characteristics of oxygen- and ozone-containing water clusters in the presence of the ions Cl^-, Br^-, and NO_3^- (Galashev 2011, 2012; Galashev et al. 2011a, b). The water or ozone (oxygen) molecule invariant in composition acts as a base unit for the water systems. Each molecule has its own electrical characteristics: permanent dipole moment $\mathbf{d}^{per}$, polarizability $\alpha^{(p)}$, and calculated induced dipole moment $\mathbf{d}^{ind}$. The compositionally stable molecules can be found neither in silicon dioxide nor in gallium nitride or gallium arsenide nor in the nanoparticle based on them. Consequently, in this case, the exact characteristics of molecules ($\mathbf{d}^{per}$, $\alpha^{(p)}$, and $\mathbf{d}^{ind}$) cannot be used for calculating the dielectric properties of nanoparticles. But the presence of covalent bonds in SiO_2, GaN, and GaAs or their combinations makes it possible to isolate the local units from some atom, surrounded by any other atoms of a nanoparticle, at each instant of time. The number of neighbors of every atom is chosen according to the assumed parameters of the interaction potential and does not exceed four, as a rule. The experimental values of polarizability were taken as 3.75, 0.793, 8.1, 1.1, and 4.3 Å^3 (Lide 1996) for the atoms of Si, O, Ga, N, and As, respectively. The permanent dipole moments of these atoms were assumed equal to zero. Considering the individual characteristics of atoms $\mathbf{d}_{atom}^{per}$ and $\alpha_{atom}^{(p)}$, one can determine the effective values of these quantities and $\mathbf{d}^{ind}$ for the local groups of atoms. Precisely, these effective characteristics of the local groups of atoms were used for calculating the dielectric properties of the nanoparticles $(SiO_2)_{86}$, $(GaX)_{129}$, and $(SiO_2)_{50}(GaX)_{54}$, where X= N or As.

The dielectric permittivity $\varepsilon(\omega)$ as a frequency ω function was presented by the complex value $\varepsilon(\omega) = \varepsilon'(\omega) - i\varepsilon''(\omega)$. For determining this value, the following equation was used (Galashev 2011, 2012):

$$\frac{\varepsilon(\omega)-1}{\varepsilon_0-1} = -\int_0^\infty \exp(-i\omega t)\frac{dF}{dt}dt = 1 - i\omega\int_0^\infty \exp(-i\omega t)F(t)dt, \quad (9)$$

where ε_0 is the static dielectric permittivity, $F(t)$ is the normalized autocorrelation function of the total dipole moment of a nanoparticle:

$$F(t) = \frac{\langle \mathbf{M}(t)\cdot\mathbf{M}(0)\rangle}{\langle \mathbf{M}^2\rangle}, \quad (10)$$

where

$$\mathbf{M}(t) = \sum_{j=1}^{N}\mathbf{d}_j(t) \quad (11)$$

is the sum of the total dipole moments of the atoms. Calculating the values $\mathbf{d}_j = \mathbf{d}_j^{per} + \mathbf{d}_j^{ind}$, for each atom, only those neighbors that interacted with this atom according to the potentials in use were taken into account.

The Raman and infrared (IR) spectra of nanoparticles were calculated by the autocorrelation functions of fluctuations of the polarizability and dipole moment, respectively. The dipole moment $\mathbf{d}_i$ and polarizability $\boldsymbol{\alpha}_i$ of i-th atom are formed due to the interaction with the surrounding atoms, and as a result, we get (Galashev et al. 2011a, b)

$$\mathbf{d}_i = \mathbf{d}_{i,0} + \boldsymbol{\alpha}_{i,0} \sum_{j \neq i} \mathbf{T}_{ij} \mathbf{d}_j, \tag{12}$$

$$\boldsymbol{\alpha}_i = \boldsymbol{\alpha}_{i,0} + \boldsymbol{\alpha}_{i,0} \sum_{j \neq i} \mathbf{T}_{ij} \boldsymbol{\alpha}_j,$$

where $\mathbf{d}_{i,0}$ and $\boldsymbol{\alpha}_{i,0}$ are the dipole moment and polarizability gained by an atom i before interaction with the renewed (as a result of thermal motion) surroundings.

Here, $\mathbf{T}_{ij}$ is the tensor of dipole–dipole interaction

$$\mathbf{T}_{ij} = \frac{1}{|r_{ij}|^3} \left(3\hat{\mathbf{r}}_{ij}\hat{\mathbf{r}}_{ij} - \mathbf{1}\right), \tag{13}$$

where $\mathbf{r}_{ij}$ is the unit vector having the direction $\mathbf{r}_i - \mathbf{r}_j$ and $\mathbf{r}_i$ и $\mathbf{r}_j$ are the positions of the centers of atoms i and j, and $\mathbf{1}$ is the unit tensor of rank 3×3. The system of Eqs. (12) was solved by the iteration method.

The scattering cross section of infrared emission was defined by the equation (Bosma et al. 1993)

$$\sigma(\omega) = \left(\frac{2}{\varepsilon_v c \hbar \eta}\right) \omega \ \tanh\left(\frac{\hbar\omega}{2kT}\right) \times \mathrm{Re} \int_0^\infty dt e^{i\omega t} \langle \mathbf{M}(t) \cdot \mathbf{M}(0) \rangle, \tag{14}$$

where η is the refractive index independent of frequency, ε_v is the dielectric permittivity of a vacuum, and c is the speed of light.

The light being depolarized, the Raman spectrum is defined by the following equation (Bosma et al. 1993):

$$J(\omega) = \frac{\omega}{(\omega_L - \omega)^4} \left(1 - e^{-\hbar\omega/kT}\right) \times \mathrm{Re} \int_0^\infty dt e^{i\omega t} \langle \Pi_{xz}(t) \Pi_{xz}(0) \rangle, \tag{15}$$

where

$$\Pi(t) \equiv \sum_{j=1}^{N} \left[\boldsymbol{\alpha}_j(t) - \langle \boldsymbol{\alpha}_j \rangle\right], \tag{16}$$

ω_L is the exciting laser frequency, Π_{xz} is the xz-component of $\Pi(t)$, and the axis x is directed along the dipole of the group of directly interacting atoms (atom j and the neighbors interacting with it).

The refraction index η and the absorption coefficient ξ are defined by the equations (Landau and Lifshitz 1984)

$$\eta = \sqrt{\frac{\varepsilon' + \sqrt{\varepsilon'^2 + \varepsilon''^2}}{2}}, \ \xi = \sqrt{\frac{-\varepsilon' + \sqrt{\varepsilon'^2 + \varepsilon''^2}}{2}}. \tag{17}$$

The coefficient ξ determines the rate of wave attenuation as it propagates in the medium.

The total number of electrons n_{el} interacting with the external electromagnetic field in a unit volume of the nanoparticle is defined by the following equation (Landau and Lifshitz 1984):

$$n_{el} = \frac{m}{2\pi^2 e^2} \int_0^\infty \omega \varepsilon''(\omega) d\omega, \tag{18}$$

where e and m are the electron charge and mass.

The particles containing SiO_2 and GaN

Bond energies in $(SiO_2)_{86}$ and $(GaN)_{129}$ particles calculated in this work were −9.6 and −4.7 eV/atom, respectively. The corresponding experimental values for α-quartz and gallium nitride with the wurtzite structure are −9.058 (Stampfl and van de Walle 1999) and −4.529 (Serrano et al. 2000). The configurations of nanoparticles containing both SiO_2 and GaN and obtained at time 100 ps are shown in Fig. 1. Packing of SiO_2, especially when these structural units are arranged externally in a nanoparticle, is closer to the amorphous state rather than α-quartz. In both cases, separate oxygen atoms become detached from Si atoms and closely approach Ga atoms. If GaN is situated in the central part of a nanoparticle, the surface layer consisting of SiO_2 is strongly inhomogeneous and contains breaks. The GaN nucleus remains sphere shaped during whole calculations. The N and Ga atoms are strongly bound with each other. During calculations, these bonds remain intact, but N atoms shift inside the GaN nucleus, and Ga atoms, outside it. If GaN is situated on the surface of a cluster, N atoms closely approach Ga atoms and do not

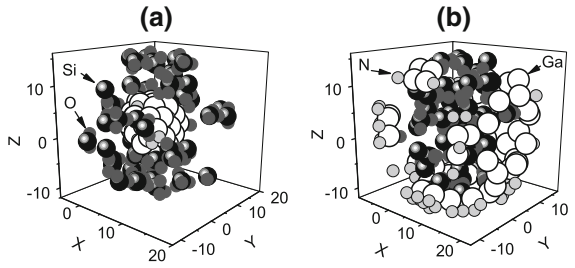

Fig. 1 Configurations of $(GaN)_{54}(SiO_2)_{50}$ nanoparticles corresponding to time 100 ps; nanoparticle nucleus is **a** GaN and **b** SiO_2

penetrate inside the cluster. Ga atoms can be in contact with both Si and O atoms. Except loss of separate O atoms, the framework of SiO_2 is retained. The inside SiO_2 nucleus has dense and loose regions. Ga atoms fairly closely approach this nucleus.

The totality of microcrystalline quartz kinds is traditionally divided into two types on the basis of crystalline habitus determined using optical microscopy (Klein and Hurlbut 1985). Granular diversities include chert and fine-grained sandstone, whereas fibrous varieties of fine-crystalline quartz are combined under a name of chalcedonies. The axis in chalcedonies is most often perpendicular to the long fiber axis. Although the majority of chalcedonies grow with just this orientation, special chalcedonies with the axis parallel to fibers or directed at an angle of 30° to them are also numerous (Folk and Pittman 1971).

The Raman spectra of the $(SiO_2)_{86}$ (α-quartz) nanoparticle, natural chalcedony from Arizona (Kingma and Hemley 1994), and a SiO_2 film (Berezhinsky et al. 2005) grown on sapphire are shown in Fig. 2. The spectra of crystalline quartz were measured at 297 ± 3 K. The low frequency region with $\omega < 50$ cm^{-1} was not considered in (Berezhinsky et al. 2005) because, according to the authors, strong spurious scattering was observed at these frequencies. The strongest bands of crystalline SiO_2 were situated at 128, 206, and 464 cm^{-1}. In addition, two bands at 696 and 808 cm^{-1} were observed. The strongest band situated at 400–530 cm^{-1} corresponds to O–Si–O symmetrical stretching-bending modes. The bands at 128 and 206 cm^{-1} correspond to torsional and O–Si–O bending modes. Recent measurements of Raman scattering from a silicon dioxide cell showed the presence of bands at 495.8 and 748.5 cm^{-1} (Schonbachler and Luthy 2010). The bands at 128 and 206 cm^{-1} are strongest in the Raman spectrum of chalcedony. Weak peaks of the same origin were observed in the J spectrum of chalcedony at 262 and 355 cm^{-1}. The SiO_2 film at $T = 293$ K consisted of the amorphous phase, but crystalline fragments were also present. The structure of SiO_2 glass is an amorphous network of Si atoms tetrahedrally surrounded by O atoms. Tetrahedra are linked with each other through oxygen atoms, and O–Si–O bridges with interbond angles close to 150° are formed. In other words, each Si atom in the amorphous network is surrounded by four O atoms, and, in turn, each oxygen atom is linked with two silicon atoms. The Raman spectrum of a SiO_2 film grown on a sapphire substrate is shown in Fig. 2, curve *4*. A broad band at about 400 cm^{-1} corresponds to Si–O tetrahedron rocking vibrations. A peak at 800 cm^{-1} was also observed. This peak was related to periodic bends of chemical bonds in O–Si–O bridges. According to (Chligui et al. 2010), an intense narrow peak at 378 cm^{-1} corresponds to plasma radiation in an Ar-laser gas discharge tube. The stoichiometry of SiO_2 is disturbed at elevated temperatures. Nonstoichiometric SiO_2 films were obtained after annealing at 773 K for 15 min. The Raman spectrum of such a film had a broad band centered at approximately 490 cm^{-1} which corresponded to Si–Si bond vibrations. This means that amorphous silicon clusters formed in the film. The first peak in the J spectrum of a low-temperature film situated at ~ 50 cm^{-1} was a wing of the Raleigh line. A well-defined low frequency peak at 34 cm^{-1} was also observed in the Raman spectrum of the $(SiO_2)_{86}$ nanoparticle. Its appearance can also be related to the presence of Raleigh scattering. The most intense broad band appears in the vicinity of a 248 cm^{-1} frequency. This band is caused by torsional vibrations and O–Si–O bending modes. As distinct from crystalline SiO_2, a large number of vibrations close in energy are observed in the $(SiO_2)_{86}$ nanoparticle in the vicinity of the 248 cm^{-1} band. Their superposition forms a broad intense Raman spectrum band. A weak burst in the J spectrum of the nanoparticle is also observed close to the 620 cm^{-1} frequency. This burst is an overtone of modes responsible for the intense Raman spectrum band at 248 cm^{-1}. The positions of the main Raman spectrum bands of the $(SiO_2)_{86}$ nanoparticle, α-quartz, and SiO_2 film are limited by the frequency range $0 \leq \omega \leq 500$ cm^{-1}. Two new Raman lines at

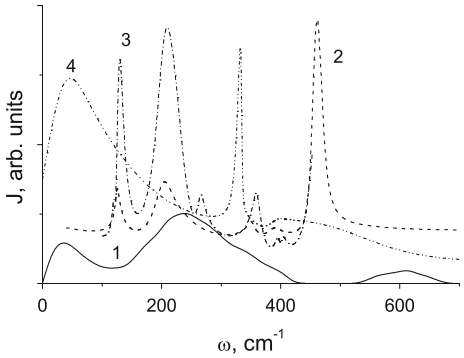

Fig. 2 Raman spectra of *1* $(SiO_2)_{86}$ nanoparticle, *2* α-quartz, *3* natural chalcedony from Arizona (Kingma and Hemley 1994), and *4* SiO_2 film grown on sapphire (Berezhinsky et al. 2005)

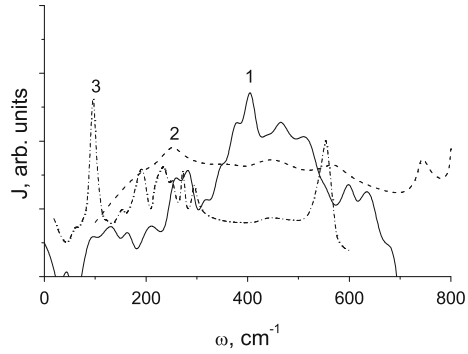

Fig. 3 Raman spectra of *1* $(GaN)_{129}$ nanoparticle and *2* GaN film grown on a sapphire substrate (Wang et al. 2006)

295 and 380 cm^{-1} and a weak mode at 605 cm^{-1} were recently observed in the Raman spectrum of amorphous silicon dioxide (Chligui et al. 2010). The authors relate the origin of the new branches to vibrations in five- and more-membered SiO_2 rings.

Because of thermal instability of gallium nitride crystals, GaN semiconductors are mainly produced and used in the form of thin films. The Raman spectrum of the GaN film grown on sapphire substrate and on GaAs is shown in Fig. 3 as well as the calculated *J* spectrum of the $(GaN)_{129}$ nanoparticle. The spectrum of the GaN film grown on sapphire has a noticeable peak at 247 cm^{-1} (Wang et al. 2006). In (Siegle et al. 1998), the origin of this peak was related to As impurities in GaN films.

This mode is present at 293 K and does not disappear upto 500 K. This is the temperature at which the beginning of the electronic transition with an increase in the number of donors is expected. The peak at 558 cm^{-1}, which appears in the Raman spectrum, corresponds to the existence of stresses in GaN films with the wurtzite structure. The E_2 additional active Raman mode is responsible for the appearance of this peak. When stresses appear, the peak shifts toward higher frequencies; its localization at 566 cm^{-1} was mentioned. The longitudinal asymmetric vibration mode is observed at 733 cm^{-1}. This mode has an obvious "tail" extended toward high frequencies. It is present in the form of a prominent signal at low temperatures. The coalescing lines at 410 and 420 cm^{-1} are acoustic overtones (Wang et al. 2006). The lines at 417 and 750 cm^{-1} related to sapphire were excluded from the spectrum. The most striking observation in (Siegle et al. 1997b) was that the additional peaks were present only in spectra taken from samples grown on GaAs. Samples grown on sapphire did not exhibit these features. For example, quite pronounced mode at 95 cm^{-1} as well as modes at 60, 102.5, 125, and 250 cm^{-1} was found in the Raman spectrum of a GaN layer grown on GaAs. The theory cannot explain all additional Raman peaks observed at low energies in GaN grown on GaAs. Either N impurities in GaAs or As defects in GaN are likely to be their origin.

The Raman spectrum of the $(GaN)_{129}$ nanoparticle is continuous and contains several bands localized at $0 \leq \omega \leq 650$ cm^{-1}. The calculated Raman spectrum of the $(GaN)_{129}$ nanoparticle has a noticeable peak of bosons (at 131 cm^{-1}) and two accompanying subpeaks at 98 and 164 cm^{-1} (Fig. 3). The boson peak is a universal special feature of the Raman spectra of most of the glasses. This peak is equally strong in many glasses and weakly changes as glass connectedness decreases. This observation was used in (McIntosh et al. 1997) to draw the conclusion that the boson peak appeared because of vibrations local in character. These vibrations can be represented by a harmonic oscillator. On the whole, the form of the spectrum of the nanoparticle corresponds to the form of the spectrum of a GaN film over the frequency range $100 \leq \omega \leq 650$ cm^{-1}. The Raman spectrum of the film has a smoother relief. The mean frequency value of nanoparticle spectrum peaks at 210, 260, and 283 cm^{-1} is 251 cm^{-1}, which closely agrees with the position of the Raman peak observed in a GaN film (247 cm^{-1}). The most intense band in the *J* spectrum of the nanoparticle at 408 cm^{-1} can be treated as an

acoustic overtone. Taking anharmonicity into account, the peaks at 464, 510, 599, and 635 cm^{-1} can be assigned to overtones of modes with a 251 cm^{-1} mean frequency. The continuous spectrum of the $(GaN)_{129}$ nanoparticle extends to $\sim$694 cm^{-1}, whereas the J spectrum of the $(SiO_2)_{86}$ nanoparticle extends to a 415 cm^{-1} frequency only; at 415 cm^{-1}, a break of the spectrum is observed. A large number of active frequencies in the Raman spectrum of the $(GaN)_{129}$ nanoparticle are caused by its small size and a small time interval during which observations were made.

The $(GaN)_{54}(SiO_2)_{50}$ nanoparticle with a GaN nucleus has a fairly smooth continuous Raman spectrum over the frequency range $0 \leq \omega \leq$ 600 cm^{-1} (Fig. 4). The band in the vicinity of a 400 cm^{-1} frequency is not most intense, as with the $(GaN)_{129}$ nanoparticle. The band situated close to a 254 cm^{-1} frequency is most intense. The intensity of the J spectrum linearly decreases as the frequency increases from 425 to 600 cm^{-1}. The Raman spectrum of the $(GaN)_{54}(SiO_2)_{50}$ nanoparticle with a SiO_2 nucleus is characterized by a substantially cut relief. This spectrum has a somewhat higher extension compared with the J spectrum of the $(GaN)_{54}(SiO_2)_{50}$ particle with a GaN nucleus. At $\omega > 559$ cm^{-1}, the Raman spectrum of the particle with a SiO_2 nucleus is not continuous. Over the frequency range $0 \leq \omega \leq 700$ cm^{-1}, the J spectrum of this particle has 11 bands. Some of these peaks (3–5) are split. The fourth peak has two subpeaks, and the third and fifth peaks have subpeaks and shoulders on the right. The first two peaks at 47 and 79 cm^{-1} should be treated as boson peaks. The position of a broad peak at 139 cm^{-1} is in agreement with the low frequency additional active Raman mode $E_2 = 144$ cm^{-1} experimentally observed in GaN films (Siegle et al. 1998). The bands at 212, 241, and 291 cm^{-1}, which have the mean frequency value 248 cm^{-1}, on the one hand, correspond to the main mode (248 cm^{-1}) of the Raman spectrum of the $(SiO_2)_{86}$ nanoparticle and, on the other hand, are close to modes with the mean frequency 251 cm^{-1} observed in the J spectrum of the $(GaN)_{129}$ nanoparticle. The band at 291 cm^{-1} is also close to a 295 cm^{-1} frequency mode in amorphous silicon (Chligui et al. 2010). In the same way, the bands at 452 and 516 cm^{-1} correspond to 464 and 510 cm^{-1} modes in the spectrum of the $(GaN)_{129}$ nanoparticle. In addition, the position of the band at

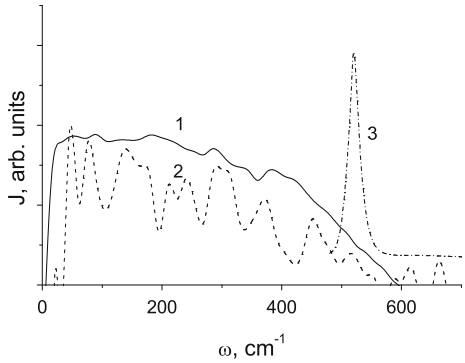

Fig. 4 Raman spectra of $(GaN)_{54}(SiO_2)_{50}$ nanoparticles with *1* GaN and *2* SiO_2 nuclei and *3* Raman spectrum of GaN/SiO_2/Si nanocrystals with a mean size of $h = 50$ nm (Konenkova et al. 2003)

516 cm^{-1} coincides with the localization of the Raman spectrum band for a GaN nanocrystal with size 50 nm grown on a SiO_2 substrate (Konenkova et al. 2003). The Raman spectrum of this nanocrystal contains only one peak (516 cm^{-1}) caused by Si atom vibrations. The position of a well-defined peak at 372 cm^{-1} is close to that of a sharp Raman spectrum peak of a SiO_2 film (378 cm^{-1}) (Berezhinsky et al. 2005) and amorphous SiO_2 (380 cm^{-1}) (Chligui et al. 2010). The other peaks at 615 and 664 cm^{-1} appear because of splitting of the peak at 620 cm^{-1} in the Raman spectrum of the $(SiO_2)_{86}$ nanoparticle. A peak close in its position (605 cm^{-1}) is also observed in amorphous SiO_2 (Chligui et al. 2010). It follows that the positions of peaks in the J spectrum of the $(GaN)_{54}(SiO_2)_{50}$ nanoparticle with a SiO_2 nucleus are caused not only by collective vibrations in the GaN subsystem but also by group vibrations in the SiO_2 subsystem.

The size of the nanoparticle as well as the number of layers in the super thin films may have some influence on the Raman spectra of samples of identical composition. The primary change is an increase in intensity of the spectra with increasing particle size and number of layers in the film. Reducing the number of layers in the film may also cause negligible (a few cm^{-1}) red or blue shift of the peaks of Raman spectrum. In the presence of strong coupling of the film to the substrate, the reduction of the film layer number can sometimes lead to the emergence of a new peak in the Raman spectrum of the bulk material. Analysis of the size dependence of the spectral

characteristics in the case of nanoparticle is complicated, as its structure with decreasing particle size changes and eventually becomes non crystal. In addition, the contribution of surface phonons is enhanced with respect to that of the bulk phonons.

The particles containing SiO_2 and GaAs

Structure

Potential energy of the $(GaAs)_{129}$ particle (at $T = 300$ K) calculated in this work was -5.4 eV. The magnitude of the cohesion energy of bulk crystal GaAs simulated by the Abell–Tersoff potential was found to be -5.78 eV (Hammerschmidt et al. 2008). The configurations of four nanoparticles obtained at $T = 1500$ K after 10^6 time steps are presented in Fig. 5. The island of oxygen atoms appeared in the top piece of nanoparticle $(SiO_2)_{86}$ at the surface. The surface of nanoparticle $(GaAs)_{129}$ is slightly disordered. The four-component nanoparticle with the core of SiO_2 still remains sufficiently compact, but the delamination of atoms Ga and As is observed at the surface. The nanoparticle with inverted arrangement of the SiO_2-component at the surface is characterized by the most loose, heterogeneous structure. In the dense central part of this nanoparticle, the bigger atoms of As dominate at the surface. The partially delaminated shell of SiO_2 is unequal in thickness and does not cover the GaAs core completely. The base units of SiO_2 do not persist. In the surface region, there are single atoms of Si and O and the base units, which are not connected to the frame: SiO, SiO_2, and SiO_4.

According to our result, crystalline $(SiO_2)_{86}$ nanoparticle has the structure of a tetrahedral network with the mean coordination number $Z_{Si-O} \approx 4$ and $Z_{Si-O} \approx 2$. The structural element of the network is a slightly distorted SiO_4 (i.e. four O atoms surround one Si atom) and the adjacent tetrahedral are linked each to other through the shared vertices. Mean O–Si–O angle is equal to 110.0° agreeing with the ideal tetrahedral structure (109.47°). This means that surface almost does not change the local order insight structural units. Oxygen atoms have a tendency to concentrate at the surface of the SiO_2 nanoparticle. Because of the excess of O atoms at the surface, Si atoms have a tendency to concentrate in the shell close to the surface. At high temperature, the $(SiO_2)_{86}$ nanoparticle acquires considerable amount of structural defects such as SiO_2 ($Z_{Si-O} = 2$), SiO_3 ($Z_{Si-O} = 3$) for Si atoms and $Z_{Si-O} = 1$ for O atoms, particularly at the surface shell.

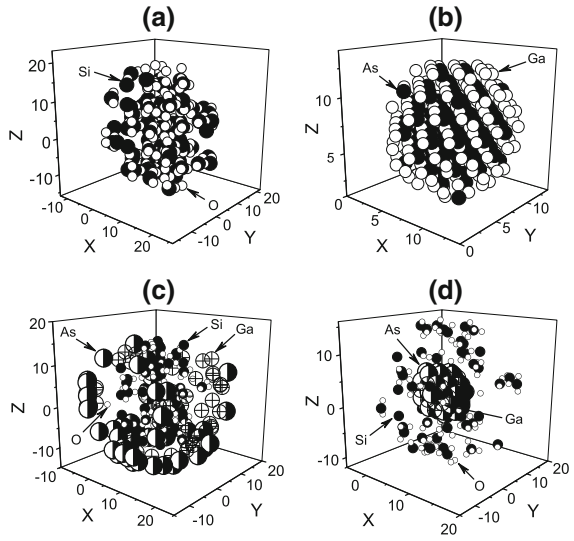

Fig. 5 Configurations of nanoparticles. **a** $(SiO_2)_{86}$; **b** $(GaAs)_{129}$; **c**, **d** $(SiO_2)_{50}(GaAs)_{54}$: **c** SiO_2 inside, **d** SiO_2 outside the nanoparticle. The coordinates of atoms are given in Å

The transition from solid to liquid phase and vice versa can be identified by a simple jump in the total potential energy curve. Equilibrium melting temperature of pure GaAs is about 1,513 K and of SiO_2 is even higher. Our calculations show that the structure of the $(GaAs)_{129}$ nanoparticle has no larger distortion caused by temperature increase. There is no evidence of the liquid state formation or mixing of atoms upto 1,500 K. Study of the detailed structure of the nanoparticles was carried out by constructing Voronoi polyhedra (VP) for its central part containing 200 atoms (Ga and As). At the temperature increase from 300 K to 1,500 K, a slight broadening of the peaks in the angular distribution of the nearest geometric neighbors was observed without displacements of their locations. As the temperature increases, the distribution of VP by the number of faces shows an increase in the number of pentahedra. And at $T = 1{,}500$ K, the share of these polyhedra is higher than the share of tetrahedra or hexahedra. However, the dominance of pentahedra is achieved solely by small-scale thermal fluctuations leading to formation of additional small faces in the tetrahedra.

When SiO_2 is represented as a nanoparticle core, the pressure of the GaAs shell increases with increase in temperature. Structural transformations in SiO_2 occur without atomic diffusion in the sense that no isolated atoms or disordered states appear at the transformation. The Si–O coordination number increases smoothly by neither breaking any Si–O bonds nor introducing global atomic diffusion. This mechanism for compression is essentially the same as that suggested by Stolper and Ahrens (1987) for amorphous silicate and is thought to occur in silica glass (Williams and Jeanloz 1988). In this case, the shell rearrangement is observed, which starts at temperature of 900 K. Note that in the temperature range of $770 \leq T \leq$ 970 K, the reconstruction of the GaAs (001) surface takes place in the physical experiment (LaBella et al. 2005). The Ga–As bond is less strong (the bond energy $E_b \approx 1.0$ eV) than the Si–O bond ($E_b \approx 11.5$ eV). More mobile atoms Ga rush into the space between the core and the shell and fill it. We can distinguish two ways to organize atoms Ga in the VI nanoparticle at high temperature. Most atoms Ga are near the SiO_2 complexes and the minority are in the vicinity of As atoms. The Ga–O and Ga–Si bonds are still poorly understood (Hinkle et al. 2009). In turn, the As atoms are grouped together (in the lower part of the VI nanoparticle). As a result, surface segregation occurs. All the atoms in the volume of nanoparticle are distributed more evenly than at the inverse geometric arrangement of the SiO_2 and GaAs components.

The temperature increase and later the dynamic atom effect of the GaAs core lead to a slight disordering of the SiO_2 structure which is a shell of the VII nanoparticle. When the SiO_2 is transformed to the slight disordering structure, the framework of the corner-shared SiO_4 is topologically rearranged, although no isolated atoms appear during the process. The coordination of silicon atoms changes. Note that the diffusion considered here does not accompany isolated atoms but is regarded as continuous changes of Si–O coordination numbers, which will require much less energy than that needed for stripping an oxygen atom from a fourfold coordinated silicon atom. In the case where GaAs consists of the nanoparticle core, there is an interlayer mixing wherein Ga atom of one layer is replaced by As atom of another layer. This leads to a collection of Ga atoms in the core interior, whereas As atoms concentrate on the core surface. Exit of As atoms to the surface is supported by the establishment of bonds with the atoms of the shell. The binding energy between O and As falls in the range of $\sim$0.10–0.20 eV (Lu et al. 2007). Consequently, O can be trapped by the As atom due to the formation of the –Si–O–Si–As complexes. This may effectively lead to a retardation of O diffusion, because O has to overcome a barrier that is equal to its binding energy in the complex in order to escape from As. The most intensive process of the As atom pushing to the surface of the core begins with the temperature of 900 K. The amplitude of vibrations of Ga and As atoms increases greater than the amplitude of Si and O atoms with temperature increase. As a result, the nanoparticle core expands more than the shell. However, even at $T = 1{,}500$ K, no one of the core atoms diffuses to the nanoparticle surface.

IR optical properties

Let us consider the general properties of the nanoparticles at the temperature of 300 K, at which the spectral characteristics of GaAs and SiO_2 films and crystals are usually obtained. In most of the frequency range, the functions $\varepsilon'(\omega)$ and $\varepsilon''(\omega)$ are increasing, i.e., the dielectric response is enhanced with the increase in the outer radiation frequency (Fig. 6). For the nanoparticles $(SiO_2)_{50}(GaAs)_{54}$ of like composition but with different component placement (*1*, VI; *2*, VII), the behavior of the frequency dependence of the real ε' and imaginary ε'' components of the dielectric permittivity at $T = 300$ K is rather identical. The values of function $\varepsilon'(\omega)$ for nanoparticles VI and VII are enclosed by the experimentally obtained values of the corresponding functions for amorphous SiO_2 (curve 3) (Tan et al. 2003) and the crystal of GaAs with the structure of zinc blende (curve 4) (Philipp and Ehrenreich 1963). At high frequencies, the smoothing of oscillations of function for particle VI is observed.

The infrared absorption spectra of nanoparticles VI and VII essentially differ in their intensity (*1*, VI, *2*, VII, Fig. 7). The intensity of the infrared spectra of the nanoparticles under consideration is mostly caused by oscillations of atoms along the ion-covalent Si–O bonds. The experimental infrared spectrum of the GaAs film (Vilcarromero et al. 2006) has fundamental peaks in the low frequency half of the range under consideration ($0 \leq \omega \leq 1{,}600$ cm^{-1}), and the major peak of the infrared spectrum of α-quartz (Ocafia et al.

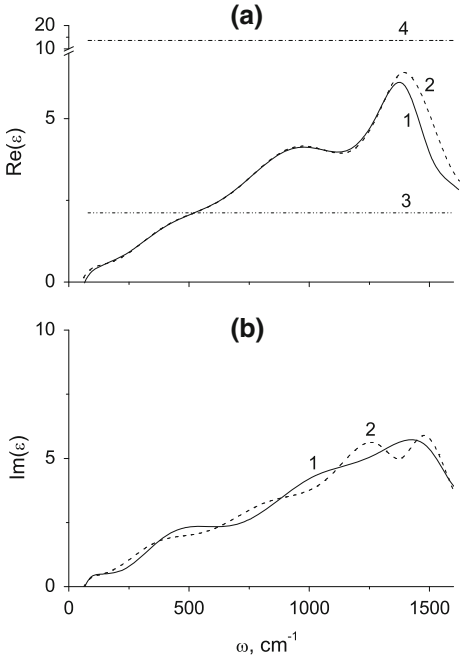

Fig. 6 The frequency dependence of real (**a**) and imaginary (**b**) components of dielectric permittivity for nanoparticles $(SiO_2)_{50}(GaAs)_{54}$: *1* VI; *2* VII; *3* amorphous SiO_2, experiment (Tan et al. 2003); *4* crystal GaAs, experiment (Philipp and Ehrenreich 1963)

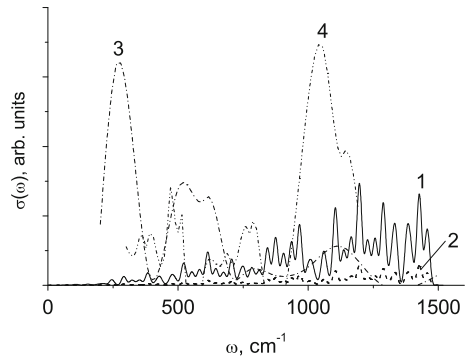

Fig. 7 The infrared absorption spectra for various systems: *1* nanoparticle VI; *2* nanoparticle VII; *3* amorphous gallium, experiment (Vilcarromero et al. 2006); *4* α-quartz, experiment (Ocafia et al. 1987)

1987) is located in the second (more high-frequency) half of this range. The intensity of the $\sigma(\omega)$ spectrum significantly increases when the surface of the nanoparticles is presented by GaAs because the hard SiO_2 shell crushes vibrations in the frequency range $\omega \leq 1{,}500$ cm $^{-1}$ and it becomes difficult to analyze such spectrum. Surface modes which exist on the crystal (100) surfaces at $\omega \leq 200$ cm^{-1} with both (1×1) and (2×1) reconstruction (Alves et al. 2004) are extremely mild in the spectrum of the nanoparticle VI. However, the first two (left), well-defined peaks corresponding to the frequencies of 245 and 290 cm^{-1}, are in good agreement with the modes (for the A irreducible representation of the point group symmetry) generated by GaAs (110) surface and localized at 250 and 288 cm^{-1}. Modes in the frequency range $300 \leq \omega \leq 1{,}000$ cm^{-1} are created not only by Ga–As dimers but also by metal-excess triatomic Ga–As–Ga clusters (Kandalam et al. 2000; Lou et al. 1992). These modes correspond to stretching symmetric (A_1) and asymmetric (B_1) Ga–As bonds. One of the stretching modes of triatomic cluster frequency is lower and the other is higher than the frequency of Ga–As monomer. Specified frequency range can be extended up to frequencies of $\sim 1{,}300$ cm^{-1}, if we take into consideration vibrations occurring in the rings formed by two dimers (Ga–As). This increases the number of active vibration modes. And mostly B-modes show quasi-degeneration. Increase of oscillation frequency with respect to dimers and triatomic cluster occurs due to the reduction in the As–As distance of the As–As/As–Ga ring. However, the greater part of the IR spectrum at $\omega > 1{,}000$ cm^{-1} is filled by modes occurring of the SiO_2 subsystem having stronger than Ga–As bonds. For the same reason, the maximum of the $\sigma(\omega)$ spectrum for α-quartz (curve 4) is in the higher frequency range than the maximum for amorphous gallium (curve 3).

As shown in Fig. 8, the infrared absorption spectra of nanoparticles VI and VII smoothed by the polynomial of the ninth degree and calculated for three temperatures. For nanoparticle VI with the SiO_2-core, the intensity I_{tot} of $\sigma(\omega)$ spectra decreases as the temperature rises (Fig. 8a). The relationship between the values of I_{tot} for temperatures 300, 900, and 1,500 K is 1:0.85:0.49. Temperature variation does not lead to shifting of the fundamental peak (on 1,380 cm^{-1}) of the $\sigma(\omega)$-spectra. The decrease in the infrared spectrum intensity with increasing temperature is caused by intensification of attenuation of the autocorrelation function of the total dipole moment. The faster attenuation of this function at high temperature is provided both by decreasing the value of $|\mathbf{M}|$ and faster change of the vector $\mathbf{M}$ direction. But the

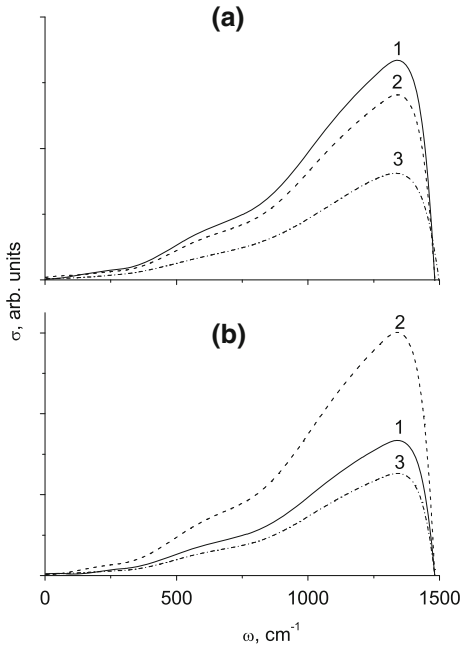

Fig. 8 The smoothed infrared absorption spectra for nanoparticles $(SiO_2)_{50}(GaAs)_{54}$ with SiO_2-core (**a**) GaAs-core (**b**) at temperatures of *1* 300 K; *2* 900 K; *3* 1,500 K

continuity of decreasing the $\sigma(\omega)$-spectrum intensity with increasing temperature is broken in the case of nanoparticle VII with external placement of the SiO_2 component. This is due to the weak impact of the GaAs-core on the outer shell of SiO_2 at $T = 300$ K. At 900 K, the loose structure of SiO_2 consolidates because the atoms of Si and O approach the GaAs-core consisting of heavier atoms. As this takes place, the distance between Si and O atoms reduces. This amplifies the Si- and O-atom oscillations. As a result, the $\sigma(\omega)$-spectrum intensity significantly increases. As temperature further rises (upto 1,500 K), the nanoparticle with a more homogenous structure behaves naturally: the infrared spectrum intensity decreases due to reducing the correlation time of the total dipole moment. The relationship between the I_{tot} values for nanoparticle VII when passing from 300 K to 900 and 1500 K is 1:1.80:0.76.

The anti-Stokes Raman spectra $J(\omega)$ for nanoparticles VI and VII essentially differ from each other not in intensity but in the number and location of peaks. In the frequency range being studied, there are observed five Raman shifts (peaks at $\omega > 0$) for nanoparticle VII and four distinguished frequency shifts for particle VI (Fig. 9). A well-resolved boson peak is observed in the low frequency portion of the Raman spectrum. In the spectrum of particles VI, the boson peak is localized at 72 cm^{-1}, whereas in the spectrum of particles VII it is at 37 cm^{-1}. Studies of reduced boson peaks in the Raman spectra of $(GaAs)_{54}(SiO_2)_{50}$ nanoparticle confirm the theoretical assumption that the shape of the peak is independent of temperature. Raman peaks of the bulk material appear when the atoms are collected in a limited amount of space, in this case, in the core of the nanoparticle. The location of the peak centered at 422 cm^{-1} in the Raman spectrum of the VI nanoparticle is close to the location of the SiO_2 nanoparticle peak (440 cm^{-1}) (Alessi et al. 2013) and that of the VII nanoparticle (240 cm^{-1}) can be correlated with the experimental peak localization (250 cm^{-1}) of the defective GaAs. The Raman peaks centered at 974 cm^{-1} (nanoparticle VI) and 650, 1,086 cm^{-1} (VII) can be correlated with experimental peaks of the SiO_2 nanoparticles at 605, and 1,060 cm^{-1}. The broadening of peaks and the low wavenumber shift of the phonon frequency of the first after boson peaks on the Raman spectra is a result of nano-sized effects. The ratio of surface area to the volume of nanoparticle is high. For this reason, it is difficult to divide the LO and TO phonons of the nanoparticle in its Raman spectrum. The experimental Raman spectrum of GaAs film at $T = 300$ K (curve *3*) was obtained up to $\omega < 700$ cm^{-1} and had two fundamental bands on the frequencies of $\sim$60 and 230 cm^{-1} (Vilcarromero et al. 2006). These bands characterize the acoustic and optical vibrational modes of amorphous GaAs, respectively. The Raman spectrum of nanoparticle VII differs significantly from the corresponding spectrum of nanoparticle VI. Recall that in this case, GaAs in the nanoparticle is a compact nanocrystal. The peak with weak intensity on $\omega = 1{,}450$ cm^{-1} in the $J(\omega)$-spectrum of nanoparticle VI can be considered as an overtone of the second mode (422 cm^{-1}) to a precision of 13 %. The fundamental peaks of the Raman spectrum of α-quartz (curve *4*) (Ocafia et al. 1987) and molten quartz (curve *5*) (Bruckner 1970) are located at the frequencies of 437 and 463 cm^{-1}, respectively. The Raman shift on 422 cm^{-1} is observed for nanoparticle VI with the center of the monolithic nanoparticle of SiO_2.

A Raman spectrum gives a set of peaks that correspond to the characteristic vibrational frequencies of the material, which can be used as a

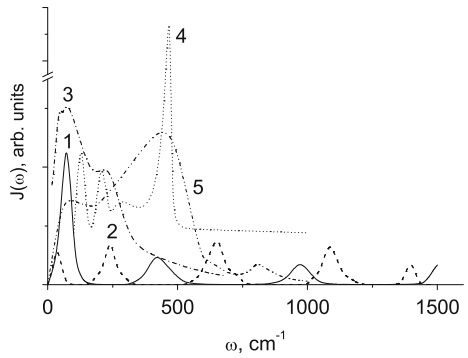

Fig. 9 The Raman spectra for various systems: *1* nanoparticle VI; *2* nanoparticle VII; *3* amorphous gallium, experiment (Vilcarromero et al. 2006); *4* α-quartz, experiment (Ocafia et al. 1987); *5* molten quartz, experiment (Bruckner 1970)

signature for identification of various materials. Each Raman emission line arises from a specific molecular bond. Experimental Raman spectra for nanoparticles (VI and VII) of such composition, i.e., is consisting of strongly binding components, is currently absent. However, new methods of the spectrum deciphering continue to evolve. For example, a detection method using the upper bound of the correlation between the target and mixing components has been presented in (Wang et al. 2012). A direct method of calculating this correlation bound is derived using observed data. The correlation bound can be used to help the independent component analysis (ICA) for detection by providing a reasonable threshold in correlation constraints. The limitation of ICA is that the mixing components have to be independent from each other, otherwise, components are split into multiple ones, decreasing the correlation with the target—if it exists in the mixture.

The temperature distinctions of the anti-Stokes Raman spectra of nanoparticles VI and VII are obvious from Fig. 10. For both nanoparticles, the Raman spectrum intensity considerably increases as the temperature rises. This is due to retarding the attenuation of the autocorrelation function of fluctuations of atomic polarizability. As the temperature rises, the polarizability deviation from the mean and the correlation time of these functions increases. The first peak of the $J(\omega)$-spectrum of nanoparticles VI and VII at $T = 300$ K is located in the range of $30 \leq \omega \leq 600$ cm^{-1}. At $T = 1{,}500$ K, the first peak of nanoparticle VII keeps its location, while for nanoparticle VI, this peak has a blue shift by ~ 50 cm^{-1}. In (Berg et al. 1990), the Raman peak at the frequency of 47 cm^{-1} was generated due to the buffer layer of GaAs, obtained by the low-temperature molecular beam epitaxy. Such a low oscillation frequency was assigned to the presence of point defects (vacancies and interstitial atoms). Such defects can be generated, for example, as a result of excess of arsenic atoms and deficiency of gallium atoms. The intensity ratio ($J^{(2)}_{1500K}/J^{(2)}_{300K}$) of the second peaks of $J(\omega)$-spectrum is 10.9 for nanoparticle VI and 9.5 for nanoparticle VII. The location of the second peak (422 cm^{-1}) of $J(\omega)$-spectrum of nanoparticle VI is almost unchanged as the temperature rises (Fig. 10a). However, the third peak has a red shift by 86 cm^{-1} at 1,500 K. Peaks 2–5 of the $J(\omega)$-spectrum of particle VII do not shift significantly under heating from 300 to 1,500 K (Fig. 10b). The more dense SiO_2-structure of nanoparticle VI as compared with the structure of nanoparticle VII leads to shifting of the Raman spectrum peaks towards higher frequencies. Not all the distinct peaks in the $J(\omega)$-spectra, obtained at 1,500 K for nanoparticles VI and VII, can reflect the fundamental frequencies of normal oscillations of atoms. For example, in the Raman spectrum of nanoparticle VI, the third and fourth peaks can reflect the overtones of the representative frequency, defined by the second peak, to a locating accuracy of 4.3 and 0.3 %, respectively. In the $J(\omega)$-spectrum of nanoparticle VII, the fifth peak can be determined accurate to 6.9 % as an overtone of the third peak frequency.

The temperature increase of the bulk materials usually leads to a decrease in frequency localization and intensity of the Raman peaks. In the case of surface-enhanced Raman scattering (SERS), the intensity of the spectrum increases significantly with increase in temperature. The exact mechanism of the enhancement effect of SERS is still a matter of debate in the literature. A similar phenomenon was observed for nanoparticles under consideration. A significant increase in the intensity of the scattering for these nanoparticles occurs through breaking of Ga-As bonds with increase of the temperature and participation of Ga atoms (and perhaps As atoms) in the vibratory process of SiO_2. The increase of the number of synchronously oscillating atoms and their total mass lead to a sharp increase in the intensity of the Raman spectrum. As the temperature of 1,500 K is not sufficiently high for SiO_2, there is a slight broadening of the Raman spectrum peaks. In this system,

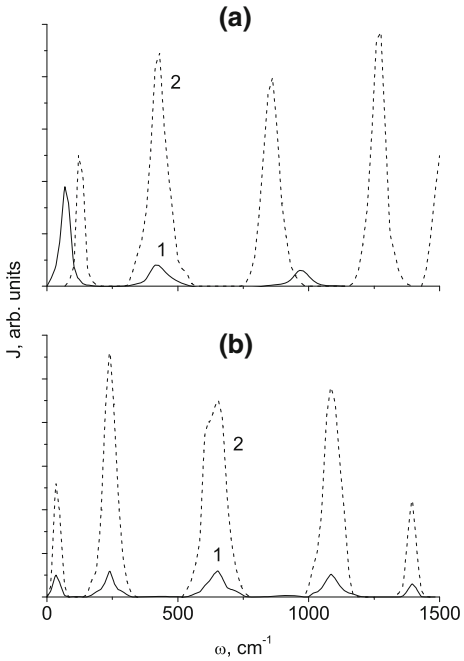

Fig. 10 The anti-Stokes spectra of Raman scattering for nanoparticles $(SiO_2)_{50}(GaAs)_{54}$ with SiO_2-core (**a**) and GaAs-core (**b**) at temperatures of *1* 300 K; *2* 1,500 K

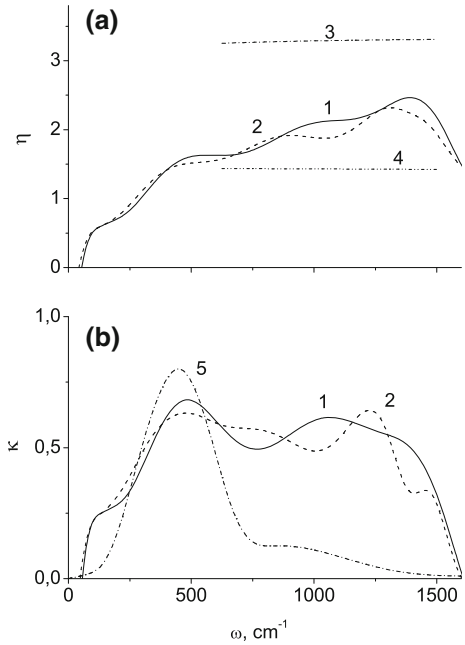

Fig. 11 The frequency dependence of refraction index (**a**) and absorption coefficient (**b**) for various systems: *1* nanoparticle VI; *2* nanoparticle VII; *3* crystal GaAs, experiment (Bass 2010); *4* amorphous SiO_2, experiment (Malitson 1965); *5* imaginary κ parts of the complex refractive index of silica glass, experiment (Kitamura et al. 2007)

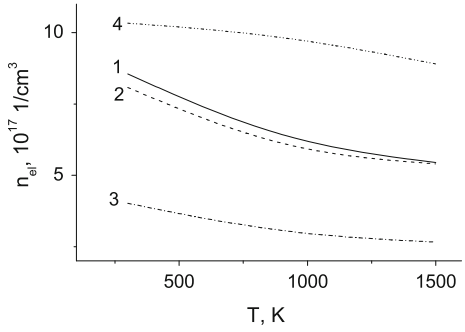

Fig. 12 The number of optically active electrons in nanoparticles: *1* VI; *2* VII; *3* I; *4* III

additionally acquired heat is eventually spent on increase of peaks' intensity.

The frequency dependences of the refraction index η and the absorption coefficient κ of nanoparticles VI and VII are of the same type (Fig. 11). But the oscillations of the $\eta(\omega)$ and $\kappa(\omega)$ functions are usually phase-shifted. The experimental values of the refraction index η of crystal GaAs (Bass 2010) (line *3*) and amorphous silicon dioxide SiO_2 (Malitson 1965) (line *4*) in the frequency range of 700 to 1,500 cm^{-1} form a band where the index η values for nanoparticles VI and VII lie. The high frequency oscillation of the $\kappa(\omega)$ function for nanopartcle VI has a lower amplitude but longer duration than the analogous feature for nanoparticle VII. The $\kappa(\omega)$ function for nanoparticles VI and VII has values close to the appropriate function of silica glass (Kitamura et al. 2007) only up to $\omega < 550$ cm^{-1} frequencies. At higher frequencies, the values of the κ coefficient of silica glass quickly decrease as the frequency increases.

The number n_{el} of electrons involved in creating optical effects decreases as the nanoparticles heat (Fig. 12). Nanoparticle VI (curve *1*) has higher values of n_{el} than nanoparticle VII. This is due to the location of Ga atoms near the nanoparticle surface. However, as the temperature rises, the difference in n_{el} values for nanoparticles VI and VII smoothes and at $T = 1{,}500$ K, it almost disappears. The number of optically active electrons is distinctly higher for the GaAs nanoparticle and lower for SiO_2 particle than for four-component nanoparticles. Nanoparticle III has a descending convex plot $n_{el}(T)$ and nanoparticle I has a concave plot like four-component nanoparticles.

Conclusions

Progress in the synthesis of high-quality nanomaterials makes it possible to investigate one of the most fundamental issues concerning the influence of the size, structure, and surface of nanoparticles on their dynamic properties including the infrared and Raman spectra. Such investigations are necessary to gain better understanding of the basic physics of controlling the parameters of nanoparticles in order to get the required dynamic properties, including the cases of thermal and mechanical load of nanoobjects.

The calculation results show that, over the larger part of the $0 \leq \omega \leq 700$ cm^{-1} frequency range, the Raman spectra of nanoparticles consisting of SiO_2 and GaN are continuous. The Raman spectrum of the $(SiO_2)_{86}$ nanoparticle is smooth and contains a wing of Raleigh scattering. Over the frequency range 420–530 cm^{-1}, a break of the spectrum is observed. Over the frequency range covered, the Raman spectrum of the $(SiO_2)_{86}$ nanoparticle is closer to the J spectrum of a SiO_2 amorphous-crystalline film than to the corresponding spectrum of crystalline or microcrystalline SiO_2. Broad Raman spectrum bands of the $(SiO_2)_{86}$ nanoparticle are formed because of overlapping of vibrational bands close in energy. The $(GaN)_{129}$ nanoparticle also has a continuous Raman spectrum. However, as distinct from the J spectrum of the $(SiO_2)_{86}$ nanoparticle, the Raman spectrum of the $(GaN)_{129}$ nanoparticle has a large number of well-defined bands. Over the frequency range $100 \leq \omega \leq 700$ cm^{-1}, the J spectrum of a GaN film with the wurtzite structure on the whole fits in with the Raman spectrum of the $(GaN)_{129}$ nanoparticle. The form of the Raman spectrum of the $(GaN)_{54}(SiO_2)_{50}$ nanoparticle depends to a substantial extent on the arrangement of components in the volume of this nanoparticle. If GaN forms its nucleus, the J spectrum has a smooth shape, and if SiO_2 occupies its center, the Raman spectrum has a large number of bands. These bands correspond to vibration of groups of atoms of different kinds and atoms of the same kind. The Raman spectrum of the nanoparticle with a SiO_2 nucleus has a larger extension, but its "tail" is not a continuous spectrum continuation.

In this paper, the basic optical properties of two- and four-component nanoparticles of silicon dioxide and gallium arsenide at temperatures of 300–1,500 K were studied. The integrated intensity of the infrared absorption spectra of four-component nanoparticles decreases as temperature rises. But the structural relaxation of the SiO_2-coating of the GaAs-core can result in increasing the intensity of this part of the infrared spectrum despite the temperature rise. The shape of Raman spectra for these particles also depends strongly on the way the GaAs- and SiO_2-components are located in the nanoparticle. Increasing the temperature of $(SiO_2)_{50}(GaAs)_{54}$ nanoparticles causes a significant rise in the intensity of the anti-Stokes part of the Raman spectrum. Heating the nanoparticles to 1,500 K does not lead to the shift of $J(\omega)$-spectrum peaks for the nanoparticle with SiO_2-coating, while the odd $J(\omega)$-spectrum peaks for the nanoparticle with the SiO_2-core shift in opposite directions. The refractive index and absorption coefficient depend weakly on the arrangement of the conductor (GaAs) and isolator (SiO_2) in the nanoparticle. The number of optically active electrons is also barely sensitive to the spatial inversion of a semiconductor and isolator in the nanoparticle formed from gallium arsenide and silicon dioxide.

Thus, using MD modeling, one can predict the significant optical properties of semiconductor particles having widespread application.

References

Agnello S, Buscarino G, Gelardi FM (2013) Raman and IR investigation of silica nanoparticles structure. J Non-Cryst Solids 362:20–24. doi:10.1016/j.jnoncrysol.2012.11.006

Alessi A, Agnello S, Buscarino G, Gelardi FM (2013) Structural properties of core and surface of silica nanoparticles investigated by Raman spectroscopy. J Raman Spectrosc 44:810–816. doi:10.1002/jrs.4292

Alves HWL, Alves JLA, Santos AM, Scolfaro LMR, Leite JR (2004) Ab initio calculation of the (100) and (110) surface phonon dispersion of GaAs and GaN. Braz J Phys 34: 617–619. doi.org/10.1590/S0103-97332004000400021

Bailon-Somintac MF, Ibanez JJ, Jaculbia RB, Loberternos RA, Defensor MJ, Salvador AA, Somintac AS (2011) Low temperature photoluminescence and Raman phonon modes of Au-catalyzed MBE-grown GaAs–AlGaAs core–shell nanowires grown on a pre-patterned Si (1 1 1) substrate. J Cryst Growth 314:268–273. doi:10.1016/j.jcrysgro.2010.10.152

Bass M (ed) (2010) Handbook of optics, vol IV. McGraw-Hill, New York

Benkabou F, Certier M, Aourag H (2003) Elastic properties of zinc-blende GaN, AlN and InN from molecular dynamics

Mol. Simul. 29:201–209. doi:10.1080/08927020210000049673

Berezhinsky LI, Maslov VP, Tetyorkin VV, Yukhymchuk VA (2005) Investigation of Al-ZERODUR interface by Raman and secondary ion mass-spectroscopy. Semiconductor Physics Quantum Electronics & Optoelectronics 8: 37–40. http://www.journal-spqeo.org.ua/n2_2005/v8n2-37-40.pdf. Accessed 22 Feb 2013

Berg RS, Mavalvala N, Steinberg T, Smith FW (1990) Raman study of defects in a GaAs buffer layer grown by low-temperature molecular beam epitaxy. J Electron Mater 19:1323–1330. doi:10.1007/BF02673349

Bhattacharya S, Datta A, Dhara S, Chakravorty D (2011) Surface optical Raman modes in GaN nanoribbons. J Raman Spectrosc 42:429–433. doi:10.1002/jrs.2704

Billeter SR, Curioni A, Fischer D, Andreoni W (2006) Ab initio derived augmented Tersoff potential for silicon oxynitride compounds and their interfaces with silicon. Phys Rev B 73:155329. doi:10.1103/PhysRevB.73.155329

Bosma WB, Fried LE, Mukamel S (1993) Simulation of the intermolecular vibrational spectra of liquid water and water clusters. J Chem Phys 98:4413–4421. doi:10.1063/1.465001

Bouzaïene L, Sfaxi L, Baira M, Maaref H, Bru-Chevallier C (2011) Power density and temperature dependent multi-excited states in InAs/GaAs quantum dots. J Nanopart Res 13:257–262. doi:10.1007/s11051-010-0024-1

Bruckner R (1970) Properties and structure of vitreous silica. J Non-Cryst Solids 5: 123–175. http://ru.scribd.com/doc/80794660/Properties-and-Structure-of-Vitreous-Silica-I. Accessed 22 Feb 2013

Chligui M, Guimbretiere G, Canizares A, Matzen G, Vaills Y, Simon P (2010) New features in the Raman spectrum of silica: Key-points in the improvement on structure knowledge. Phys Rev B. http://hal.archive-suvertes.fr/docs/00/52/08/23/PDF/ chliguiSiO2.pdf. Accessed 22 Feb 2013

Folk RL, Pittman JS (1971) Length-slow chalcedony: a new testament for vanished evaporates. J Sediment Petrol 41:1045–1058. doi:10.1306/D42687BB-2B26-11D7-8648000102C1865D

Galashev AY (2010) Simulation of silicon nanoparticles stabilized by hydrogen at high temperatures. J Nanopart Res 12:3003–3018. doi:10.1007/s11051-010-9892-7

Galashev AY (2011) Computer study of absorption of oxygen and ozone molecules by water clusters with Cl^- and Br^-. Can J Chem 89:524–533. doi:10.1139/V10-174

Galashev AY (2012) Molecular dynamics simulation of adsorption of ozone and nitrate ions by water clusters. High Temp 50:204–213. doi:10.1134/S0018151X12010051

Galashev AY, Rakhmanova OR, Novruzova OA (2011a) Molecular-dynamic modeling of the spectral characteristics of the ozone–water cluster system. High Temp 49:193–198. doi:10.1134/S0018151X11010056

Galashev AY, Rakhmanova OR, Novruzova OA (2011b) Computational study of interaction of bromine ions with clusters $(O_2)_6(H_2O)_{50}$ and $(O_3)_6(H_2O)_{50}$. High Temp 49:528–538. doi:10.1134/S0018151X11040080

Goldman RS, Briner BG, Feenstra RM, O'Steen ML, Hauenstein RJ (1996) Atomic-scale structure and electronic properties of GaN/GaAs superlattices. Appl Phys Lett 69: 3698. doi:10.1063/1.117193

Hammerschmidt T, Kratzer P, Scheffler M (2008) Analytic many-body potential for InAs/GaAs surface and nanostructures: formation energy of InAs quantum dots. Phys Rev B 77:235303. doi:10.1103/PhysRevB.81.159905

Hinkle CL, Milojevic M, Brennan B, Sonnet AM, Aguirre-Tostado FS, Hughes GJ, Vogel EM, Wallace RM (2009) Detection of Ga suboxides and their impact on III-V passivation and Fermi-level pinning. Appl Phys Lett 94: 162101. doi:10.1063/1.3120546

Jayaraman A, Wood DL, Maines RG (1987) High-pressure Raman study of the vibrational modes in aluminum phosphate and a-quartz. Phys Rev B 35:8316–8321. doi:10.1103/PhysRevB.35.8316

Jiang D-S, Ramsteiner M, Ploog K-H, Tews H, Graber A, Averbeck R, Riechert H (1998) Defect-induced Raman scattering in resonance with yellow luminescence transitions in hexagonal GaN on a sapphire substrate. Appl Phys Lett 72:365–368. doi:10.1063/1.120738

Kaczmarczyk G, Kaschner A, Hoffmann A, Thomsen C (2000) Impurity-induced modes of Mg, As, Si, and C in hexagonal and cubic GaN. Phys Rev B 61:5353–5357. doi:10.1103/PhysRevB.61.5353

Kandalam AK, Pandey R, Blanco MA, Costales A, Recio JM, Newsam JM (2000) First principles study of polyatomic clusters of AlN, GaN, and InN. 1. Structure, stability, vibrations, and ionization. J Phys Chem B 104:4361–4367. doi:10.1021/jp994308s

Kim JS, Kim EK, Song JD, Choi WJ, Lee JI (2006) Study on the energy-band structure of an InAs/InGaAs/GaAs Quantum-dot infrared photodetector structure. J Korean Phys Soc 49:2124–2127. doi:10.3938/jkps.49.2132

Kingma KJ, Hemley RJ (1994) Raman spectroscopic study of microcrystalline silica. Am Mineral 79:269–273

Kitamura R, Pilon L, Jonasz M (2007) Optical constants of silica glass from extreme ultraviolet to far infrared at near room temperature. Appl Optics 46:8118–8133. doi:10.1364/AO.46.008118

Klein C, Hurlbut CS Jr (1985) Manual of Mineralogy, 20th edn. Wiley, New York

Konenkova EV, Zhilyaev YuV, Fedirko VA, Zahn DRT (2003) Raman spectroscopy of GaN nucleation and free-standing layers grown by hydride vapor phase epitaxy on oxidized silicon. Appl Phys Lett 83:629–631. doi:10.1063/1.1592623

Kozawa T, Kachi T, Kano H, Taga Y, Hashimoto M, Koide N, Manabe K (1994) Raman scattering from LO phonon-plasmon coupled modes in gallium nitride. J Appl Phys 75:1098–1101. doi:10.1063/1.356492

Landau LD, Lifshitz EM (1984) Electrodynamics of continuous media. Course of theoretical physics, vol 8. Butterworth–Heinemann, Oxford

LaBella VP, Krause MR, Ding Z, Thibado PM (2005) Arsenic-rich GaAs(0 0 1) surface structure. Surf Sci Rep 60:1–53. doi:10.1016/j.surfrep.2005.10.001

Le Bail A (2005) Inorganic structure prediction with GRINSP. J Appl Crystallogr 38:389–395. doi:10.1107/S0021889805002384

Lide DR (ed) (1996) CRC Handbook of chemistry and physics, 77th edn. CRC Press, Boca Raton-Florida

Lou L, Norland P, Smalley RE (1992) Electronic structure of small GaAs clusters. J Chem Phys 97: 1858–1864. doi.org/10.1063/1.463174

Lu G-H, Wang Q, Liu F (2007) First-principles calculation of interaction between interstitial O and As dopant in heavily As-doped Si. J Appl Phys 101:026104. doi:10.1063/1.2423231

Malitson IH (1965) Interspecimen comparison of the refractive index of fused silica. J Opt Soc Am 55:1205–1208. doi:10.1364/JOSA.55.001205

McIntosh C, Toulouse J, Tick P (1997) The Boson peak in alkali silicate glasses. J Non-Cryst Solids 222:335–341. doi:10.1016/S0022-3093(97)90133-2

McMillan PF, Hess AC (1990) Ab initio valence force field calculations for quartz. Phys Chem Miner 17:97–107. doi:10.1007/BF00199660

Metin CO, Lake LW, Miranda CR, Nguyen OP (2011) Stability of aqueous silica nanoparticle dispersions. J Nanopart Res 13:839–850. doi:10.1007/s11051-010-0085-1

Mooradian A, Wright GB (1966) First order Raman effect in III–V compounds. Solid State Commun 4: 431–434. http://dx.doi.org/10.1016/0038-1098(66)90321-8

Munetoh S, Motooka T, Moriguchi K, Shintani A (2007) Interatomic potential for Si–O systems using Tersoff parameterization. Comput Mater Sci 39:334–339. doi:10.1016/j.commatsci.2006.06.010

Nayak J, Mythili R, Vijayalakshmi M, Sahu SN (2004) Size quantization effect in GaAs nanocrystals. Physica E 24: 227–233. http://dx.doi.org/10.1016/j.physe.2004.04.035

Nishidate Y, Nikishkov GP (2008) Atomic-scale modeling of self-positioning nanostructures. Comput Model Eng Sci 26:91–106. doi:10.3970/cmes.2008.026.091

Nordlund K, Peltola J, Nord J, Keinonen J, Averback RS (2000) Defect clustering during ion irradiation of GaAs: insight from molecular dynamics simulations. J Appl Phys 90:1710–1717. doi:10.3970/cmes.2008.026.91

Ocafia M, Fornes V, Garcia-Ramos JV, Serna CJ (1987) Polarization effects in the infrared spectra of α-quartz and α-cristobalite. Phys Chem Miner 14:527–532. doi:10.1007/BF00308288

Okuyama K, Lenggoro IW (2003) Preparation of nanoparticles via spray route. Chem Eng Sci 58:537–547. doi:10.1016/S0009-2509(02)00578-X

Philipp HR, Ehrenreich H (1963) Optical properties of semiconductors. Phys Rev 129:1550–1560. doi:10.1103/PhysRev.129.1550

Ramsteiner M, Menniger J, Brandt O, Yang H, Ploog KH (1996) Shallow donors in GaN studied by electronic Raman scattering in resonance with yellow luminescence transitions. Appl Phys Lett 69:1276–1278. doi:10.1063/1.117390

Schonbachler N, Luthy W (2010) Measurements of Raman lines in silica, dimethyl_methylphosphonate and methyl salicylate. Univ Bern Press, Bern

Serrano J, Rubio A, Hernandez E, Muñoz A, Mujica A (2000) Theoretical study of the relative stability of structural phases in group-III nitrides at high pressures. Phys Rev B 62:16612–16623. doi:10.1103/PhysRevB.62.16612

Siegle H, Loa I, Thurian P, Kaczmarczyk G, Filippidis L, Hoffmann A, Thomsen C (1997a) Defect modes and disorder induced Raman scattering in GaN. Z Phys Chem 200:187–193. doi:10.1524/zpch.1997.200.Part_1_2.187

Siegle H, Loa I, Thurian P, Eckey L, Hoffmann A, Broser I, Thomsen C (1997b) Comment on "Shallow donors in GaN studied by electronic Raman scattering in resonance with yellow luminescence transitions" [Appl. Phys. Lett. 69,1276 (1996)]. Appl Phys Lett 70:909. doi:10.1063/1.119072

Siegle H, Kaschner A, Hoffmann A, Broser I, Thomsen C, Einfeldt S, Hommel D (1998) Raman scattering from defects in GaN: the question of vibrational or electronic scattering mechanism. Phys Rev B 58:13619–13626. doi:10.1103/PhysRevB.58.13619

Stampfl C, van de Walle CG (1999) Density-functional calculations for III-V nitrides using the local-density approximation and the generalized gradient approximation. Phys Rev B 59:5521–5535. doi:10.1103/PhysRevB.59.5521

Stolper EM, Ahrens TJ (1987) On the nature of pressure-Induced coordination changes in silicate melts and glasses. Geophys Res Lett l4:1231–1233. doi:10.1029/GL014i012p01231

Tan G-L, Lemon MF, French RH (2003) Optical properties and London dispersion forces of amorphous silica determined by vacuum ultraviolet spectroscopy and spectroscopic ellipsometry. J Am Ceram Soc 86:1885–1892. doi:10.1111/j.1151-2916.2003.tb03577.x

Tersoff J (1986) New empirical model for the structural properties of silicon. Phys Rev Lett 56:632–635. doi:10.1103/PhysRevLett.56.632

Tersoff J (1989) Modeling solid-state chemistry: interatomic potentials for multicomponent systems. Phys Rev B 39:5566–5568. doi:10.1103/PhysRevB.39.5566

Vassileva E, Furuta N (2001) Application of high-surface-area ZrO_2 in preconcentration and determination of 18 elements by on-line flow injection with inductively coupled plasma atomic emission spectrometry. Fresenius J Anal Chem 370:52–59. doi:10.1007/s002160100744

Vilcarromero J, Bustamante R, Silva JHD (2006) Hydrogen influence on gallium arsenide thin films prepared by rf-magnetron sputtering technique. Braz J Phys 36: 1035–1037. doi:10.1590/S0103-97332006000600063

Wang R-M, Chen G-D, Lin J-Y, Jiang H-X (2006) Comparative analysis of temperature-dependent Raman spectra of GaN and GaN/Mg films. Front Phys China 1:112–116. doi:10.1007/s11467-005-0007-3

Wang W, Adali T, Emge D (2012) A novel approach for target detection and classification using canonical correlation analysis. J Signal Process Syst 68:379–390. doi:10.1007/s11265-011-0625-7

Williams Q, Jeanloz R (1988) Spectroscopic evidence for pressure-induced coordination changes in silicate glasses and melts. Science 239:902–905. doi:10.1126/science.239.4842.902

Yasukawa A (1996) Using an extended Tersoff interatomic potential to analyze the static–fatigue strength of SiO_2 under atmospheric influence. Jpn Soc Mech Eng Int J 39: 313–320. http://www.jsme.or.jp/English/. Accessed 22 Feb 2013

Zheleva TS, Ashmawi WM, Nam O-H, Davis RF (1999) Thermal mismatch stress relaxation via lateral epitaxy in selectively grown GaN structures. Appl Phys Lett 74: 2492–2494. doi:10.1063/1.123017